Effect of geometry and orientation on the tensile properties and failure mechanisms of compliant suture joints

*Amir Darabi [a], Rong Long [b], Joel C. Weber [c], and Lewis M. Cox [a]**

[a] Department of Mechanical & Industrial Engineering, Montana State University, 220 Roberts Hall, Bozeman, MT, 59717, USA

[b] Department of Mechanical Engineering, University of Colorado Boulder, 1111 Engineering Drive, Boulder, CO, 80309, USA

[c] National Institute of Standards and Technology, 325 Broadway, Boulder, CO, 80305, USA

KEYWORDS: Compliant interlayers, suture joints, geometric interlayer, mechanics of composites, crack growth stability, photopolymers

ABSTRACT: Compliant sutures surrounded by stiff matrices are present in biological armors and carapaces, providing enhanced mechanical performance. Understanding the mechanisms through which these sutured composites achieve outstanding properties is key to developing engineering materials with improved strength and toughness. This article studies the impact of suture geometry and load direction on the performance of suture joints using a two-stage reactive polymer resin that enables facile photopatterning of mechanical heterogeneity within a single polymer network.

Compliant sinusoidal sutures with varying geometries are photopatterned into stiff matrices, generating a modulus contrast of two orders of magnitude. Empirical relationships are developed connecting suture wavelength and amplitude to composite performance under parallel and perpendicular loading conditions. Results indicate that a greater suture interdigitation broadly improves composite performance when loading is applied perpendicular to suture joints, but has deleterious effects when loading is applied parallel to the joint. Investigations into the failure mechanisms under perpendicular loading highlight the interplay between suture geometry and crack growth stability after damage initiation occurs. Our findings could enable a framework for engineering composites and bio-inspired structures in the future.

1. INTRODUCTION

Biological composites have long piqued the interest of researchers as their mechanical properties often exceed those of their constituent materials.[1,2] The underlying architecture of mechanical heterogeneity in biological composites has generally been shown to improve performance through a variety of mechanisms such as crack bridging, crack deflection, and microcracking.[3–7] One design element commonly observed in biological structures is the compliant, geometrically patterned interlayers, known as sutures, connecting regions of stiffer, mineralized materials.[8] Sutures are widely implemented by flora and fauna manifesting at length scales ranging from nanometers to millimeters, found in the cranial and facial bones of white-tailed deer and many other large mammals,[9,10] within the protective carapace of red-eared slider turtles,[11] in the beak of red-bellied woodpecker,[12] between the shell and septum of ammonoid phragmocone,[13–15] and in the seedcoat of *Portulaca oleracea*.[16]

Broadly considered to impart flexibility, impact resistance, enhanced strength, and improved toughness, the explicit mechanisms governing the performance of sutured composites remain largely unknown, but interest is growing. Modeling stress fields around sutures with simplified triangular and rectangular shapes subjected to perpendicular loads provided early evidence that suture geometry greatly influences stress transfer,[17] while subsequent studies on the inclusion of mechanically interlocking sutures enhanced toughness and strain to failure after damage initiation.[18,19] However, investigations into fundamental geometry-performance relationship of wavy, sinusoidal suture joints common in biocomposites are limited. Recent work employing extrusion-based multi-material printing has characterized suture performance in lap shear, relating a single-variable description of suture waviness to mechanical performance.[20] The same article also has highlighted the manufacturing challenges associated with suture research by identifying and characterizing the non-trivial impact that the printing direction of extrusion nozzles has on the sub-millimeter defect structure, failure mechanisms, and macroscopic composite performance. Despite exciting advancements, a fundamental understanding of the relationship between the suture geometry and composite performance under complex loading conditions remains largely absent.[21]

We seek to erode a portion of this knowledge gap by leveraging multi-material photopolymer resin that provides spatial control over heterogeneity without introduction of defects in order to develop empirical geometry-performance relationships in suture joints under parallel and perpendicular loading orientations. We employ a two-stage reactive polymer (TSRP) that provides spatiotemporal tuning of crosslinking density within a continuous network, enabling a two order of magnitude variation in Young's moduli to be photopatterned into a network without introducing defects or discontinuities across heterogeneous domains.[22–25] However, while the potential for layer-by-layer printing of TSRPs has been demonstrated,[26,27] significant development is still required before 3D voxel control can be realized. Therefore, our use of the TSRP system will be confined to film with a thickness on the order of 100 μm, consistent with established TSRP use in literature.[28–30] Specifically, this study investigates how the amplitude (A), wavelength (λ) and associated index of suture complexity (ISC) relate to the modulus, strength, and toughness of films containing a single sinusoidal suture joint when subjected to tensile loads perpendicular and parallel to the suture axis. The empirical relationships developed in this study provide a novel design framework for future composites utilizing suture joints for enhanced performance.

2. MATERIALS AND METHODS

Suture geometries: Seven different suture geometries were selected for study, including six sinusoidal patterns and one flat line serving as the control. The linewidth of the suture is fixed at 100 μm for all samples. The sinusoidal patterns include two different wavelengths (λ) and three different amplitudes (A, **Figure 1**). A convenient parameter used in literature that captures a combined effect of these two variables is the dimensionless index of sutural complexity (*ISC*),[31]

$$ISC = \frac{contour\ length\ of\ suture\ line}{contour\ length\ of\ flat\ line\ suture}. \tag{1}$$

Therefore, a flat line "suture" exhibits an ISC of 1, the minimum possible value. Table S1 in supporting appendix describes the different geometric parameters studied.

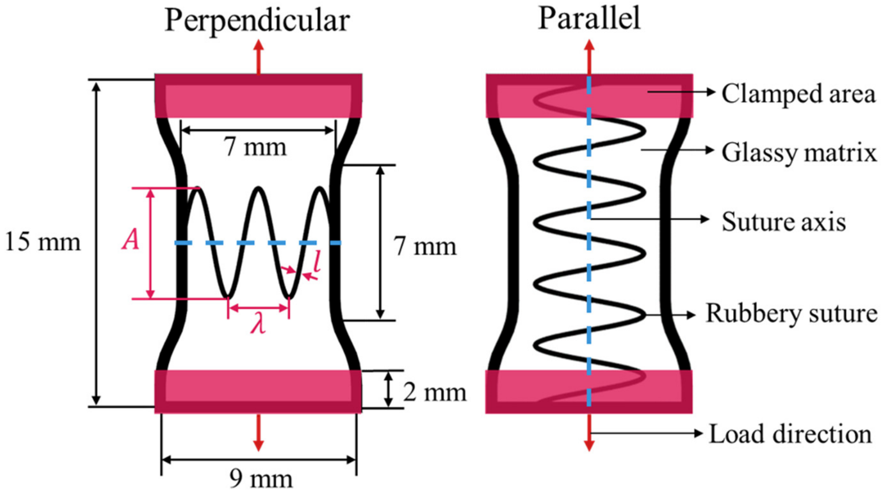

Figure 1. A representation of an ISC-3.8 suture (Table S1) with suture axis perpendicular (left) and parallel (right) to the load direction. A is showing the amplitude, λ the wavelength, and l the linewidth of the suture sine wave.

Clamping dimensions, working space, and photo-processing resolution dictate the upper and lower bounds of the geometric parameters selected for this study. However, the dimensions investigated in this study are relevant to modern manufacturing capabilities and are comparable to the length scales of certain, though not all, biological suture joints.[8,32,33] The suture patterns were lithographically defined on a chrome-etched photomask.

Film processing: The selected TSRP formulation is comprised of pentaerythritol tetrakis(3-mercaptopropionate) mixed with a 1:2.75 functional group excess of trimethylolpropane triacrylate. Triethyl amine (0.1 wt%) serves as the catalyst for the first stage thiol Michael addition “click” reaction that is allowed to run to conversion overnight and produces a rubbery material. The photoinitiator 2,2-Dimethoxy-2- phenylacetophenone (1.5 wt%) initiates the second stage, free-radical acrylate homopolymerization reaction upon UV exposure (OmniCure S1500 lamp, 300 nm – 400 nm wavelength filter, 30 mW cm^{-2} intensity for 30 sec) and produces a glassy material. The inhibitor butylated hydroxytoluene (0.05 wt%) was added to improve shelf life and to mitigate partial curing under the photomask. Structural formulae of compounds used in this study are shown in Figure S1. Prior to UV exposure, the top surface of samples was laminated against the photomask, the bottom surface was capped with a stoichiometric TSRP film to prevent oxygen inhibition, and the resulting sandwich placed over a black felt-lined box to prevent light reflection from degrading pattern fidelity. A representation of the second stage polymerization experimental setup, along with an image of the photomask are shown in Figure S2.

Photomask designs embed sutures inside a dog bone outline with two different orientations (Figure 1). The dog bone outline is 0.5 mm thick and, after photopatterning, provided a rubbery border around the glassy composite matrix that allowed samples to be easily cut out without introducing cracks into the rigid matrix. Resulting composite films had a thickness of 80 ± 20 μm.

3. RESULTS

A minimum of five samples per geometry were analyzed using a dynamic mechanical analysis instrument (DMA, TA instruments Q800) with an applied quasi-static strain rate of 2% per minute. The constituent materials of the composite are referred to as the rubber (forming the suture) and the glass (forming the matrix). Prior to investigating composite performance, monolithic samples of the homogeneous, isotropic rubber and glass materials were characterized. The rubber exhibited inferior modulus (2.64 ± 0.88 MPa against 638.20 ± 128.90 for glass), strength (0.47 ± 0.15 MPa against 18.76 ± 3.39 for glass), and toughness (7.87 ± 4.79 (J cm^{-3}) against 82.14 ± 30.66 (J cm^{-3}) for glass), a useful contrast when differentiating the impacts of suture geometry from changes in material volume fraction of composite samples.

3.1 Modulus

The moduli for the monolithic rubbery and glassy materials, as well as the apparent moduli of the composite films are illustrated in **Figure 2a** and 2b for suture joints oriented perpendicular and parallel to the tensile loading, respectively. Mean rubber and glass moduli are shown with dashed lines and a grey box indicating the 25th and 75th percentile of the measurements (rubber percentiles are negligible relative to the axis scaling). When loading is applied perpendicular to the suture joint, the apparent moduli of all films lie between the values of the constituent materials but exhibit a slight upward trend as ISC increases. This result is noteworthy as the modest increase in composite modulus corresponds to a 20-fold increase in the volume fraction of rubber, which grows from 0.6% at the lowest ISC to 12% at the highest ISC. This elevation in modulus can be partially rationalized using an unconventional adaptation of the transformation relations proposed for unidirectional fiber composites, also known as fiber laminate theory (FLT).[30,34] FLT traditionally predicts a unidirectional fibrous composite stiffness as a function of fiber orientation relative to applied loads (Equation S1). Here, we applied this model to predict the mechanical properties of our composite films after certain assumptions and simplifications (Figure S3). While imperfect, FLT broadly captures the slight upward trend of composite modulus despite increasing rubber content. From both FLT and experimental data, we infer that the composite response stiffens under perpendicular loading as the suture path becomes increasingly oriented along the loading axis.

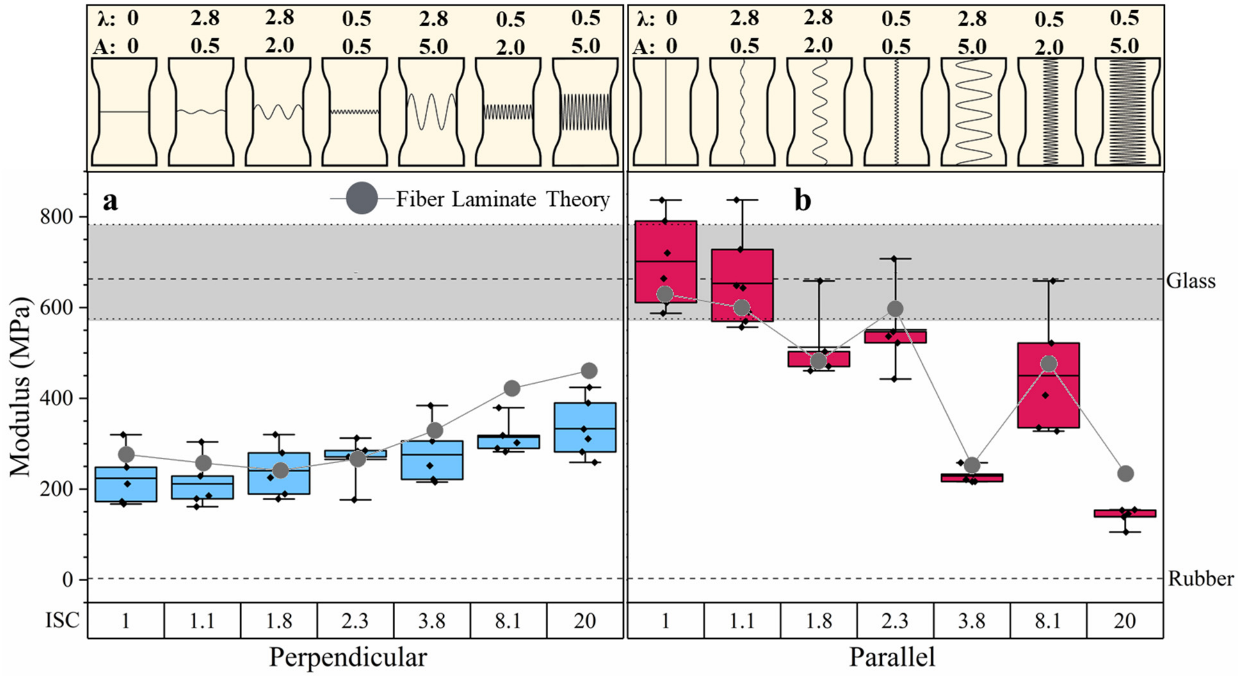

Figure 2. Modulus of composites with different suture joint geometries when oriented a) perpendicular and b) parallel to the loading direction. Modulus predictions of fiber laminate theory (FLT) are shown for both loading conditions.

The measured moduli under parallel loading conditions exhibit a much stronger dependency on suture geometry (Figure 2b). Despite the unconventional adaptation and the underlying simplicity of FLT, the model exhibits a striking, though imperfect, ability to describe the experimental performance of suture joints under parallel loading. Multiple linear regression (MLR) was used to determine the relationship between the sutured films moduli and the amplitude (A) and wavelength (λ) of the sinusoidal sutures under both loading conditions. Moduli of sutured films were normalized by the modulus of the flat line sutures for each loading direction, and the amplitude and wavelength of the sinusoidal sutures were normalized by the length of the flat line suture, h. All measured mechanical properties were log-transformed to satisfy MLR assumptions. Empirical relationships correlating modulus to suture amplitude and wavelength are shown in **Equation 2 and 3** for perpendicular and parallel loading conditions, respectively. [36–38]

$$\mathrm{Ln}\left(\frac{E_{ISC,\perp}}{E_{1,\perp}}\right) = \frac{0.44}{h_{\perp}}(A) \tag{2}$$

$$\mathrm{Ln}\left(\frac{E_{ISC,\parallel}}{E_{1,\parallel}}\right) = \frac{-4.42}{h_{\parallel}}(A - 0.24\lambda) \tag{3}$$

In above equations, E_1 is the apparent modulus of the film with a flat-line suture joint. No term for λ is present in Equation 2 as MLR determined its impact to be not significant under perpendicular loading ($F_{1,30} = 3.53, p - value = 0.07$). In addition, single linear regression (SLR) was used to determine the relationship between modulus and ISC for perpendicular loading condition, which resulted in a slightly less accurate model than the one obtained by MLR (Table S2). A final point of interest in the modulus data is that the ISC-3.8 sample exhibits no statistically significant difference in its response to the two loading orientations, indicating suture geometry enables accentuation or mitigation of anisotropy.

3.2 Toughness

Here, toughness is defined as the total work to fracture under tensile loading (W_T) and is calculated using the area under a stress-strain curve (unit: J cm^{-3}).[36] The toughness for the monolithic rubber and glass materials, as well as the toughness of the sutured films are shown in **Figure 3a** and 3b for perpendicular and parallel loading conditions, respectively. In Figure 3a, the toughness for ISC-1 under perpendicular loading is noticeably lower than the toughness of a monolithic rubber, which is expected due to significantly higher local strain along the suture than the matrix when loaded in this configuration.[37] As ISC increases, toughness increases, exceeding that of the rubbery material at ISC-3.8. The trend of increasing toughness with ISC is generally consistent with theory in literature that identifies the term A/λ (analogous to ISC), as a key parameter for the toughening mechanism of suture joints.[38,39] A related and noteworthy observation is that despite the significant increase in the volume fraction of low-toughness rubber with increasing ISC, the toughness of the sutured film also increases. The toughness of ISC-20 films (89.14 ± 20.26 J cm^{-3}) is strikingly 5 times that of the ISC-8.1 geometry (17.36 ± 5.67 J cm^{-3}), 50 times of the ISC-1 geometry (1.59 ± 0.50 J cm^{-3}) and exhibits no statistical difference from the toughness of the monolithic glass (see supporting information).

$$\mathrm{Ln}\left(\frac{W_{ISC,\perp}}{W_{1,\perp}}\right) = \frac{5.42}{h_{\perp}}(A - 0.46\lambda) \tag{4}$$

SLR model of toughness as a function of ISC is also provided in the supporting information, Table S2. While the accuracy of both MLR and SLR models is comparable, MLR is presented over SLR since sutures with different geometries may share the same ISC value.

When the suture joint is oriented parallel to the tensile load, only the ISC-3.8 sample fails to meet or exceed the toughness of the monolithic glass, Figure 3b. Similar to trends observed in modulus measurements, toughness of sutured films under parallel tensile loading conditions is dominated by amplitude, while the influence of wavelength is minor. The empirical relationship between suture geometry and composite toughness for parallel suture joints was obtained using multiple linear regression, **Equation 5**.

$$\mathrm{Ln}\left(\frac{W_{ISC,\parallel}}{W_{1,\parallel}}\right) = \frac{-5.10}{h_{\parallel}}(A + 0.36\lambda) \tag{5}$$

Based on this equation, composite toughness under parallel loads monotonically decreases with increasing suture amplitude and, for a fixed amplitude, lower wavelength sutures exhibit larger toughness values than their higher wavelength counterpart. Specifically, at a constant amplitude of 2 mm or 5 mm, lower wavelengths yield higher toughness values. This study tests only two different suture wavelengths, limiting the analysis that can be performed, but it is possible that sufficiently low suture wavelengths will render the toughness of composites insensitive to suture amplitude under parallel loading conditions,[8,9] enabling the toughening mechanism related to high ISC values under perpendicular loading conditions to be captured without deleterious tradeoffs in complex loading environments. Additional work is needed to explore this exciting possibility.

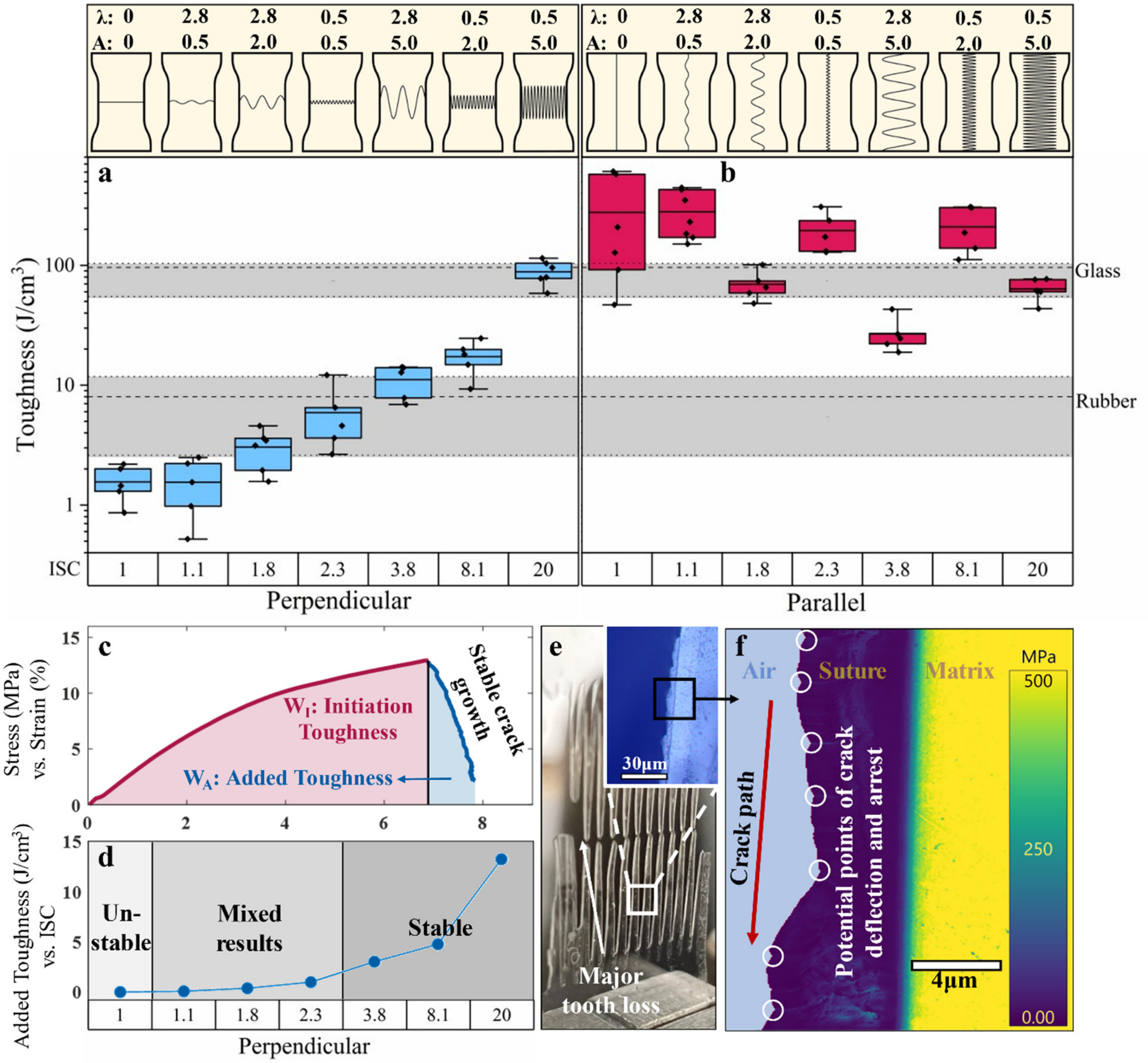

Figure 3. Toughness of composites with different suture joint geometries when oriented a) perpendicular and b) parallel to the loading direction. c) Stress-strain curve of an ISC-20 sample at a strain rate of 2% min^{-1}. The total toughness (work to fracture) is separated into initiation toughness and added toughness due to crack arrest. d) Mean added toughness for suture joints with respect to ISC, for perpendicular sutures. Crack growth stabilizes as ISC increases. e) An image of a fractured ISC-20 film, with a representation of major tooth loss. The inset of (e) shows an optical image of the fracture interface containing large scallop features – scale bar indicates 30µm. f) An AFM modulus map corresponding to the optical inset of (e) demonstrates that the crack remains within the rubber and highlights small scallop features.

To better understand the relationship between toughness and failure phenomena, stress-strain curves are broken up into two categories helpful for describing damage evolution. The first category is initiation toughness, defined as the energy stored before crack initiation, and is highlighted in the red region of the representative ISC-20 dataset in Figure 3c. The second category is added toughness, defined as the additional energy needed to induce failure after crack initiation, and is highlighted in the blue region of Figure 3c. The portion of the curve bounding the added toughness corresponds to a regime of stable crack growth. For perpendicular loading conditions only, all films exhibit cohesive failure of the rubber material, guiding cracks along the inside of the suture during failure. Crack guiding is a known toughening mechanism observed in hierarchical biological materials.[21] For a flat line ISC-1 suture, crack propagation is unstable and catastrophic failure occurs immediately after crack initiation, corresponding to an added toughness of zero. However, crack propagation begins to stabilize with increasing ISC (Figure 3d). For smaller ISC values spanning 1.1 and 2.3, half of tested samples showed brief but discernable stability in crack propagation, providing a minor amount of added toughness. For ISC values of 3.8 and higher, stable crack propagation was observed in every tested sample. Contrasting instances of crack instability and stability can be observed in videos capturing failure of ISC-1, ISC-1.8, and ISC-20 samples (supporting videos SV1, SV2 and SV3, respectively). The added toughness accompanying crack growth stability is considerable and monotonically increases with ISC, accounting for as much as 27% of the total work to fracture for the ISC-3.8 and ISC-8.1 composites.

The fractured surfaces of sutured films were studied with optical and atomic force microscopy (AFM, Asylum Research Cypher S). Optical images show periodic, micrometer-scale scallops along the fracture interface of samples exhibiting stable crack growth (inset of Figure 3e). Modulus maps (AFM fast force mapping, 300 Hz rate, 40 N m^{-1} tip, Tap300Al-G, BudgetSensors) confirm that under perpendicular loading conditions, mixed-mode cohesive fracture of the rubber is the dominant failure mechanism (Figure 3f), a phenomenon consistent with previous studies of crack guiding in TSRPs,[30] although exceptions to the dominant cohesive failure of rubber do arise, here referred to as "tooth loss." Tooth loss occurs when a crack temporarily leaves the rubbery suture, propagates across the glass, and re-enters the suture on the opposite side of the tooth. The phenomenon arises at two very distinct length scales. Major tooth loss is defined as any crack departure from the rubber that occurs further than 100 μm from the suture peak (Figure 3e, and an optical image in Figure S4a). Major tooth loss may occur in any suture geometries, excluding ISC-1, but is rare, occurring across less than 5% of all suture teeth.

Minor tooth loss, not discernable by the naked eye, is identified when departure from the rubber occurs within 100 μm of a suture peak (Figure S4b). Minor tooth loss only occurs in the ISC-8.1

and ISC-20 samples but is observed around 75% of all suture peaks within these two suture geometries.

When suture joints are parallel to the loading, failure becomes considerably more complex (Figure S5). In these arrangements, cracks must bisect the sample, travelling perpendicular to the loading direction and interacting with both the rubbery suture and the glassy matrix. In addition to horizontally bisecting the sample during failure, when the suture amplitude is 2 mm and lower cracks may become entrenched in the suture and travel vertically along its axis. Samples with a suture amplitude of 5 mm (ISC-20 and ISC-3.8) prevent cracks from moving more than half of a suture wavelength in the vertical direction. When significant vertical crack propagation does occur, cracks move beyond the narrow neck of the dog bone sample and potentially interact with the clamp, where boundary conditions influence performance. It is noted that while significant variations in crack nucleation loci and crack pathing arose in all sample geometries, crack nucleation was not observed to occur at the clamp itself. However, nucleation was observed by eye and high-speed videography would be required to accurately describe failure loci. Clamping is therefore considered to have no impact on modulus values, since they are measured at low strains prior to damage. Similarly, the influence of boundary conditions on values of initiation toughness and strength are considered negligible since these values correspond to the instant that damage initiation occurs in all sample geometries (maximum stress is always observed immediately prior to damage initiation) and clamp interactions are observed to occur after damage initiation. However, clamping effects have an unknown impact on calculations of added toughness under parallel loading. As a final point regarding toughness measurements, the insensitivity of ISC-3.8 films to loading direction is once again apparent.

3.3 Strength

Trends in strength, reported as maximum tensile stress, are similar to those of toughness for both loading orientations. Under perpendicular loading, strength increases with ISC, reaching 14.22 MPa for the ISC-20 sample, just below that of the monolithic glass (**Figure 4a**). Under parallel loading, strength again decreases as suture amplitude increases, (Figure 4b), and wavelength has an even weaker influence on strength than on toughness. Comparing composite strength between the two loading conditions, the ISC-3.8 geometry is once again noteworthy as it exhibits equivalent strength under both loading directions.

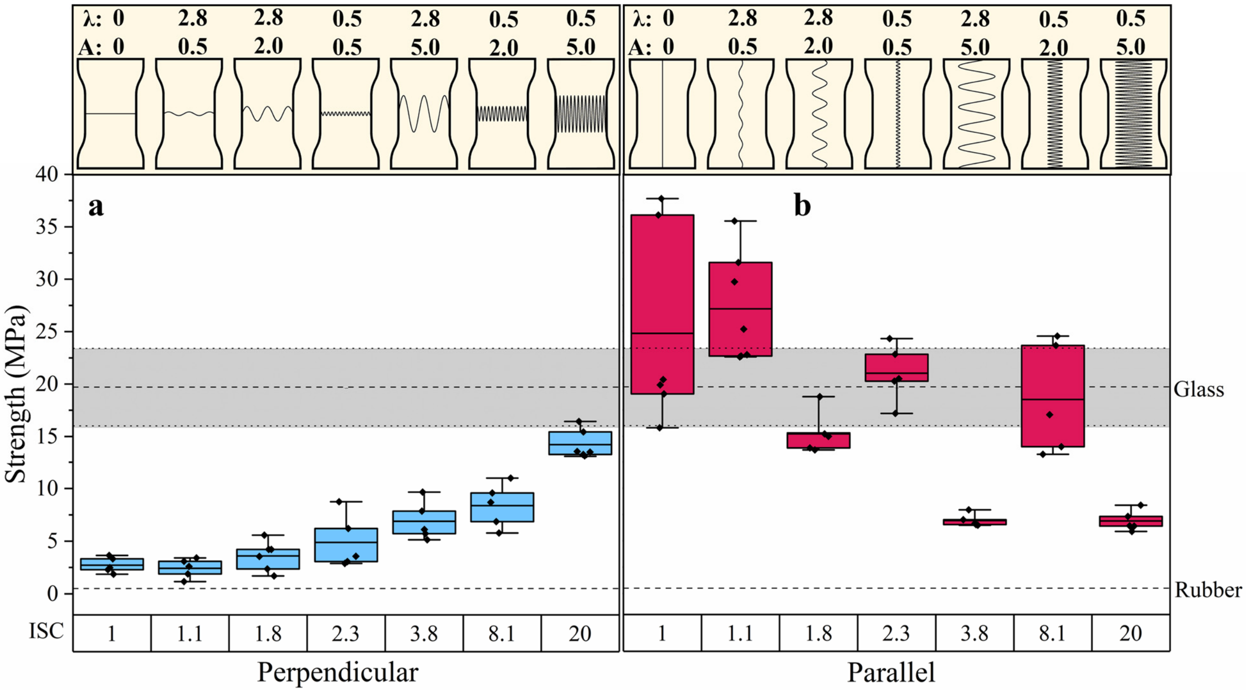

Figure 4. The strength of composites with different suture joint geometries when oriented a) perpendicular and b) parallel to the load direction.

MLR was used to correlate the suture geometry to composite performance, similar to toughness and modulus. **Equation 6 and 7** describe the relationship between composite strength and joint geometry for perpendicular and parallel loading condition, respectively.

$$\mathrm{Ln}\left(\frac{\sigma_{ISC,\perp}}{\sigma_{1,\perp}}\right) = \frac{2.37}{h_{\perp}}(A - 0.51\lambda) \tag{6}$$

$$\mathrm{Ln}\left(\frac{\sigma_{ISC,\parallel}}{\sigma_{1,\parallel}}\right) = \frac{-3.99}{h_{\parallel}}(A - 0.16\lambda) \tag{7}$$

4. DISCUSSION

All empirical relationships developed to describe geometry-performance relationships in suture joints under tension are collected in **Table 1**. Coefficient α describes the sensitivity of a mechanical property to changes in geometry, and coefficient β represents the relative effects of wavelength and amplitude. Since increasing amplitude and decreasing wavelength corresponding to higher ISC values, contrasting signage attached to these variables represent synergistic contributions, while similar signage indicates competing contributions. The degree to which these empirical relationships can be extended beyond the parameter space tested is not known, but one limitation is anticipated: If the geometric parameters (including line width which is fixed at 100 μm in this study) are implemented at length scales comparable to the crack tip opening displacement and its associated processing zone, it is reasonable to expect that changes in crack tip stress fields will result in deviations from the relationships developed here.

Table 1. Empirical relationships for the mechanical properties of composites with different suture joint geometries.

Mechanical property (Y)	Suture orientation (θ)	$\mathrm{Ln}\left(\frac{Y_{ISC,\theta}}{Y_{1,\theta}}\right) = \frac{\alpha}{h}(A + \beta\lambda)$

		$h(mm)$	α	β
Modulus	Perpendicular, $\perp$	7	0.44	0
Toughness	Perpendicular, $\perp$	7	5.42	-0.46
Strength	Perpendicular, $\perp$	7	2.37	-0.51
Modulus	Parallel, $\parallel$	15	-4.42	-0.24
Toughness	Parallel, $\parallel$	15	-5.10	0.36
Strength	Parallel, $\parallel$	15	-3.99	-0.16

5. CONCLUSION

The relationship between suture geometry and the mechanical properties of composites were explored using a TSRP platform that enables photopatterning of mechanical heterogeneity without introduction of defects or manifestation of poor adhesion across material domains. Several combinations of wavelength and amplitude were considered in the sinusoidal sutures and ISC was employed to describe the combined impacts of those two variables. Sutured film performance was characterized under tensile loads with suture joints oriented perpendicular and parallel to the load direction. When loading is applied perpendicular to axis, composite moduli are largely insensitive to suture geometry. However, both strength and toughness increase with elevated ISC, despite the increased volume fraction of the suture's mechanically poor rubber material, opposing traditional strength and toughness trade-offs in composite design.[7] Under this perpendicular loading, failure evolves with ISC, where unstable crack propagation transitions to stable propagation and crack trapping as ISC is increased, corresponding to monotonically increasing values of added toughness.

When loading is applied parallel to the suture axis, amplitude dominates composite performance, with smaller values providing enhanced modulus, strength, and toughness. Although the effect of ISC is not as significant as amplitude for parallel sutures, at a constant amplitude, lower wavelengths (higher ISCs) exhibit lower modulus, similar strength, and higher toughness compared to their higher wavelength (lower ISC) counterparts. Failure mechanisms under parallel loading conditions were significantly more complex.

Comparing between loading orientations, the strength, toughness, and modulus for every suture geometry, excluding ISC-20, was either superior under parallel loading conditions or equivalent between the two. ISC-20 is the only suture geometry that consistently performed better under perpendicular loads, while the ISC-3.8 geometry was uniquely insensitive to loading orientation. While imperfect, modulus results for both loading orientations could be largely captured using an unconventional adaption of FLT. Despite the assumptions underlying this theory, it shows promise as a useful tool for predicting the stiffness of sutured composites.

For both loading conditions, empirical relationships were developed, as seen in Table 1, relating suture amplitude and wavelength to the mechanical performance of composites with sinusoidal sutures with respect to a flat-line suture. The developed scaling relationships in this work provide a framework for predicting the mechanical response of composites with suture joints of different geometries and orientations.

ASSOCIATED CONTENT

Supporting Information

Supporting Information is available free of charge.

Additional details regarding theoretical assumptions underlying use of the fiber laminate theory model, structural formulae of compounds, experimental setup during film processing, and images and videos of composite failure are available in Supporting Information.

AUTHOR INFORMATION

Corresponding Author

* Lewis M. Cox - E-mail: lewis.cox@montana.edu

Notes

The authors declare no conflict of interest.

ACKNOWLEDGMENTS

The authors thank Prof. Chelsea Heveran at Montana State University for assistance with statistical analysis. We acknowledge funding support from the National Science Foundation under grant numbers CMMI-2038512 and CMMI-2038505. This work represents the views of the authors and not necessarily those of the sponsors.

REFERENCES

(1) Wegst, U. G. K.; Bai, H.; Saiz, E.; Tomsia, A. P.; Ritchie, R. O. Bioinspired Structural Materials. *Nat Mater* **2015**, *14* (1), 23–36.

(2) Barthelat, F.; Tang, H.; Zavattieri, P. D.; Li, C. M.; Espinosa, H. D. On the Mechanics of Mother-of-Pearl: A Key Feature in the Material Hierarchical Structure. *J Mech Phys Solids* **2007**, *55* (2), 306–337.

(3) Sistaninia, M.; Kolednik, O. Improving Strength and Toughness of Materials by Utilizing Spatial Variations of the Yield Stress. *Acta Mater* **2017**, *122*, 207–219.

(4) Chen, I. H.; Yang, W.; Meyers, M. A. Leatherback Sea Turtle Shell: A Tough and Flexible Biological Design. *Acta Biomater* **2015**, *28*, 2–12.

(5) Wang, Y. Q.; Fritz, R.; Kiener, D.; Zhang, J. Y.; Liu, G.; Kolednik, O.; Pippan, R.; Sun, J. Fracture Behavior and Deformation Mechanisms in Nanolaminated Crystalline/Amorphous Micro-Cantilevers. *Acta Mater* **2019**, *180*, 73–83.

(6) Fischer, F. D.; Kolednik, O.; Predan, J.; Razi, H.; Fratzl, P. Crack Driving Force in Twisted Plywood Structures. *Acta Biomater* **2017**, *55*, 349–359.

(7) Ritchie, R. O. The Conflicts between Strength and Toughness. *Nat Mater* **2011**, *10* (11), 817–822.

(8) Naleway, S. E.; Porter, M. M.; McKittrick, J.; Meyers, M. A. Structural Design Elements in Biological Materials: Application to Bioinspiration. *Advanced Materials* **2015**, *27* (37), 5455–5476.

(9) Nicolay, C. W.; Vaders, M. J. Cranial Suture Complexity in White-Tailed Deer (Odocoileus Virginianus). *J Morphol* **2006**, *267* (7), 841–849.

(10) Jaslow, C. R. Mechanical Properties of Cranial Sutures. *J Biomech* **1990**, *23* (4), 313–321.

(11) Krauss, S.; Monsonego-Ornan, E.; Zelzer, E.; Fratzl, P.; Shahar, R. Mechanical Function of a Complex Three-Dimensional Suture Joining the Bony Elements in the Shell of the Red-Eared Slider Turtle. *Advanced Materials* **2009**, *21* (4), 407–412.

(12) Lee, N.; Horstemeyer, M. F.; Rhee, H.; Nabors, B.; Liao, J.; Williams, L. N. Hierarchical Multiscale Structure - Property Relationships of the Red-Bellied Woodpecker (Melanerpes Carolinus) Beak. *J R Soc Interface* **2014**, *11* (96), 20140274.

(13) Inoue, S.; Kondo, S. Suture Pattern Formation in Ammonites and the Unknown Rear Mantle Structure. *Sci Rep* **2016**, *6*, 33689.

(14) Li, Y.; Ortiz, C.; Boyce, M. C. Bioinspired, Mechanical, Deterministic Fractal Model for Hierarchical Suture Joints. *Phys Rev E Stat Nonlin Soft Matter Phys* **2012**, *85* (3), 1–14.

(15) Lin, E.; Li, Y.; Weaver, J. C.; Ortiz, C.; Boyce, M. C. Tunability and Enhancement of Mechanical Behavior with Additively Manufactured Bio-Inspired Hierarchical Suture Interfaces. *J Mater Res* **2014**, *29* (17), 1867–1875.

(16) Gao, C.; Hasseldine, B. P. J.; Li, L.; Weaver, J. C.; Li, Y. Amplifying Strength, Toughness, and Auxeticity via Wavy Sutural Tessellation in Plant Seedcoats. *Advanced Materials* **2018**, *30* (36), 1–8.

(17) Li, Y.; Ortiz, C.; Boyce, M. C. Stiffness and Strength of Suture Joints in Nature. *Phys Rev E Stat Nonlin Soft Matter Phys* **2011**, *84* (6), 062904.

(18) Lin, E.; Li, Y.; Ortiz, C.; Boyce, M. C. 3D Printed, Bio-Inspired Prototypes and Analytical Models for Structured Suture Interfaces with Geometrically-Tuned Deformation and Failure Behavior. *J Mech Phys Solids* **2014**, *73*, 166–182.

(19) Mirkhalaf, M.; Dastjerdi, A. K.; Barthelat, F. Overcoming the Brittleness of Glass through Bio-Inspiration and Micro-Architecture. *Nat Commun* **2014**, *5*, 1–9.

(20) Nash, R. J.; Li, Y. Experimental and Numerical Analysis of 3D Printed Suture Joints under Shearing Load. *Eng Fract Mech* **2021**, *253* (July), 107912.

(21) Huang, W.; Restrepo, D.; Jung, J. Y.; Su, F. Y.; Liu, Z.; Ritchie, R. O.; McKittrick, J.; Zavattieri, P.; Kisailus, D. Multiscale Toughening Mechanisms in Biological Materials and Bioinspired Designs. *Advanced Materials* **2019**, *31* (43), 1–37.

(22) Nair, D. P.; Cramer, N. B.; McBride, M. K.; Gaipa, J. C.; Shandas, R.; Bowman, C. N. Enhanced Two-Stage Reactive Polymer Network Forming Systems. *Polymer* **2012**, *53* (12), 2429–2434.

(23) Podgórski, M.; Nair, D. P.; Chatani, S.; Berg, G.; Bowman, C. N. Programmable Mechanically Assisted Geometric Deformations of Glassy Two-Stage Reactive Polymeric Materials. *ACS Applied Materials and Interfaces* **2014**, *6* (9), 6111–6119.

(24) Blevins, A. K.; Wang, M.; Lehmann, M. L.; Hu, L.; Fan, S.; Stafford, C. M.; Killgore, J. P.; Lin, H.; Saito, T.; Ding, Y. Photopatterning of Two Stage Reactive Polymer Networks with CO2-Philic Thiol-Acrylate Chemistry: Enhanced Mechanical Toughness and CO2/N2 Selectivity. *Polym Chem* **2022**, *13* (17), 2495-2505.

(25) Munch, E.; Launey, M. E.; Alsem, D. H.; Saiz, E.; Tomsia, A. P.; Ritchie, R. O. Tough, Bio-Inspired Hybrid Materials. *Science (1979)* **2008**, *14* (1), 32–50.

(26) Kuang, X.; Zhao, Z.; Chen, K.; Fang, D.; Kang, G.; Qi, H. J. High-Speed 3D Printing of High-Performance Thermosetting Polymers via Two-Stage Curing. *Macromol Rapid Commun* **2018**, *39* (7), 1700809.

(27) Kuang, X.; Wu, J.; Chen, K.; Zhao, Z.; Ding, Z.; Hu, F.; Fang, D.; Qi, H. J. Grayscale Digital Light Processing 3D Printing for Highly Functionally Graded Materials. *Sci Adv* **2019**, *5* (5), 1–10.

(28) Blevins, A. K.; Cox, L. M.; Hu, L.; Drisko, J. A.; Lin, H.; Bowman, C. N.; Killgore, J. P.; Ding, Y. Spatially Controlled Permeability and Stiffness in Photopatterned Two-Stage Reactive Polymer Films for Enhanced CO2 Barrier and Mechanical Toughness. *Macromolecules* **2021**, *54* (1), 44–52.

(29) Nair, D. P.; Cramer, N. B.; McBride, M. K.; Gaipa, J. C.; Lee, N. C.; Shandas, R.; Bowman, C. N. Fabrication and Characterization of Novel High Modulus, Two-Stage Reactive Thiol-Acrylate Composite Polymer Systems. *Macromol Symp* **2013**, *329* (1), 101–107.

(30) Cox, L. M.; Blevins, A. K.; Drisko, J. A.; Qi, Y.; Ding, Y.; Fiedler-, C. I.; Long, R.; Bowman, C. N.; Killgore, J. P.; Cox, L. M.; Killgore, J. P. Tunable Mechanical Anisotropy, Crack Guiding, and Toughness Enhancement in Two- Stage Reactive Polymer Networks. *Adv Eng Mater* **2019**, *21* (8), 1900578.

(31) de Blasio, F. V. The Role of Suture Complexity in Diminishing Strain and Stress in Ammonoid Phragmocones. *Lethaia* **2008**, *41* (1), 15–24.

(32) Lee, N.; Williams, L. N.; Mun, S.; Rhee, H.; Prabhu, R.; Bhattarai, K. R.; Horstemeyer, M. F. Stress Wave Mitigation at Suture Interfaces. *Biomed Phys Eng Express* **2017**, *3* (3), 035025.

(33) Alheit, B.; Bargmann, S.; Reddy, B. D. Dynamic Mechanical Behaviour of Suture Interfaces as Inspiration for Architectured Hierarchical Interlocking Composites. *J Mech Phys Solids* **2021**, *157*, 104620.

(34) Daniel, I. M.; Ishai, O. *Engineering Mechanics of Composite Materials*, 2nd ed.; Oxford University Press: New York, **2006**, 77-87.

(35) Tham, M. W.; Fazita, M. N.; Abdul Khalil, H. P. S.; Mahmud Zuhudi, N. Z.; Jaafar, M.; Rizal, S.; Haafiz, M. M. Tensile Properties Prediction of Natural Fibre Composites Using Rule of Mixtures: A Review. *Journal of Reinforced Plastics and Composites* **2019**, *38* (5), 211–248.

(36) Ritchie, R. O.; Koester, K. J.; Ionova, S.; Yao, W.; Lane, N. E.; Ager, J. W. Measurement of the Toughness of Bone: A Tutorial with Special Reference to Small Animal Studies. *Bone* **2008**, *43* (5), 798–812.

(37) Hosseini, M. S.; Cordisco, F. A.; Zavattieri, P. D. Analysis of Bioinspired Non-Interlocking Geometrically Patterned Interfaces under Predominant Mode I Loading. *J Mech Behav Biomed Mater* **2019**, *96*, 244–260.

(38) Zavattieri, P. D.; Hector, L. G.; Bower, A. F. Determination of the Effective Mode-I Toughness of a Sinusoidal Interface between Two Elastic Solids. *Int J Fract* **2007**, *145* (3), 167–180.

(39) Zavattieri, P. D.; Hector, L. G.; Bower, A. F. Cohesive Zone Simulations of Crack Growth along a Rough Interface between Two Elastic-Plastic Solids. *Eng Fract Mech* **2008**, *75* (15), 4309–4332.

For table of contents use only

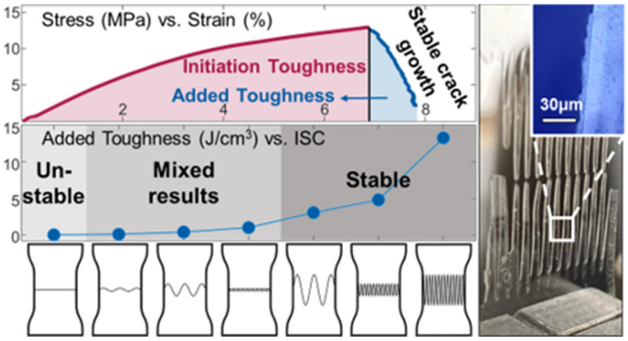

Supporting Information

Effect of geometry and orientation on the tensile properties and failure mechanisms of compliant suture joints

Amir Darabi [a], *Rong Long* [b], *Joel C. Weber* [c], *and Lewis M. Cox* [a]*

[a] Department of Mechanical & Industrial Engineering, Montana State University, 220 Roberts
Hall, Bozeman, MT, 59717, USA

[b] Department of Mechanical Engineering, University of Colorado Boulder, 1111 Engineering
Drive, Boulder, CO, 80309, USA

[c] National Institute of Standards and Technology, 325 Broadway, Boulder, CO, 80305, USA

* Corresponding author: lewis.cox@montana.edu

Photoprocessing of Composite Films

Table S1. Index of suture complexity (ISC) related to wavelength, amplitude, and contour length.

ISC	λ (mm)	A (mm)	Contour length, perpendicular (mm)	Contour length, parallel (mm)
1	-	-	7	15
1.1	2.8	0.5	7.5	16.1
1.8	2.8	2	12.6	26.8
2.3	0.5	0.5	16.1	34.6
3.8	2.8	5	26.4	56.9
8.1	0.5	2	56.8	121.7
20	0.5	5	140.4	300.8

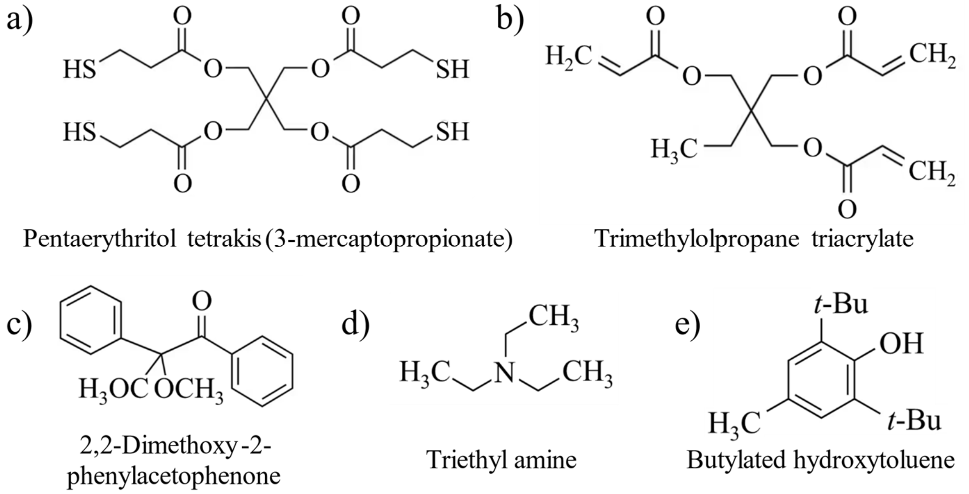

Pentaerythritol tetrakis (3-mercaptopropionate)

Trimethylolpropane triacrylate

2,2-Dimethoxy-2-phenylacetophenone

Triethyl amine

Butylated hydroxytoluene

Figure S1. Structural formulae and names of the a,b) monomers used to form the network backbone, formulated with a 1:2.75 (thiol:acrylate) off-stoichiometric functional group ratio, c) free radical photoinitiator, d) catalyst for thiol-michael polymerization, and d) inhibitor present to mitigate spurious crosslinking events.

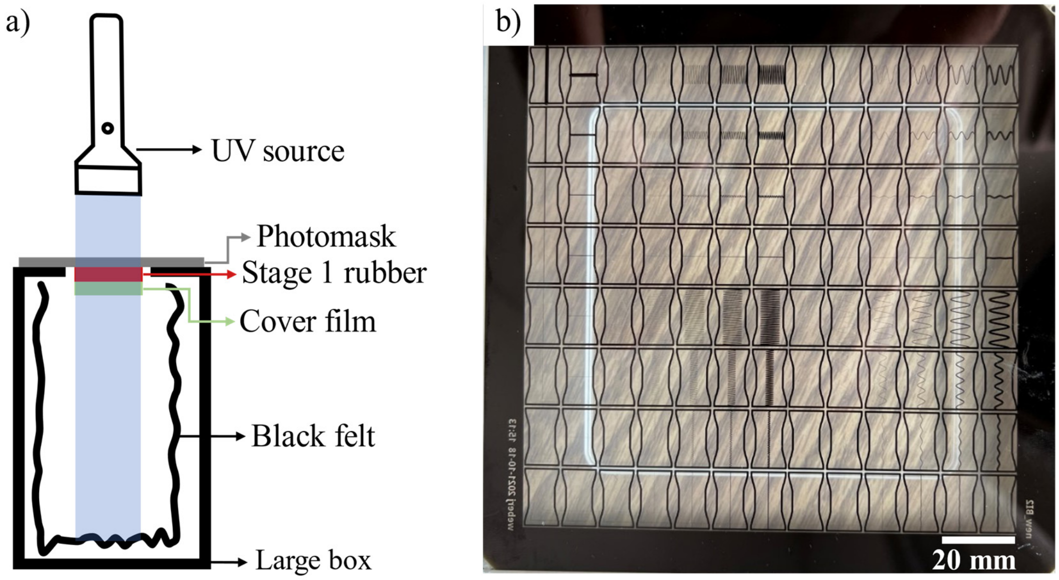

Figure S2. a) Rubbery films are laminated against a photomask on top and against a cover film on bottom to prevent oxygen inhibition. Transmitted UV light passes through the sample and is captured in a box lined with black felt to mitigate reflection. b) Picture of the mask used for photopatterning samples. Not all geometries depicted were used in this study.

Fiber Laminate Theory

Fiber laminate theory (FLT) models the modulus of fiber composites as a function of fiber orientation with respect to loading condition according to the relationship:

$$\frac{1}{E_\theta} = \frac{m^2}{E_1}(m^2 - n^2 v_{12}) + \frac{n^2}{E_2}(n^2 - m^2 v_{21}) + \frac{m^2 n^2}{G_{12}}. \tag{S1}$$

In this equation, $\boldsymbol{m} = \mathbf{cos}\,\boldsymbol{\theta}$ and $\boldsymbol{n} = \mathbf{sin}\,\boldsymbol{\theta}$ with $\boldsymbol{\theta}$ representing the orientation of fiber with respect to the load, $\boldsymbol{G_{12}}$ is the shear modulus along the fiber orientation, $\boldsymbol{E_1}$ and $\boldsymbol{E_2}$ are the tensile modulus along and perpendicular to the fiber orientation, respectively, and $\boldsymbol{v_{12}}$ and $\boldsymbol{v_{21}}$ are the Poisson's ratio associated with angle of 0 and 90 degrees between the fiber and the applied tensile load, respectively. The mechanical parameters, i.e., $\boldsymbol{G_{12}}$, $\boldsymbol{E_1}$, $\boldsymbol{E_2}$, $\boldsymbol{v_{12}}$ and $\boldsymbol{v_{21}}$, are calculated based on the rule of mixtures, as shown below.

$$v_{12} = V_f v_f + V_m v_m \tag{S2}$$

$$\frac{1}{v_{21}} = V_f \frac{1}{v_f} + V_m \frac{1}{v_m} \tag{S3}$$

$$E_1 = V_f E_f + V_m E_m \tag{S4}$$

$$\frac{1}{E_2} = V_f \frac{1}{E_f} + V_m \frac{1}{E_m} \tag{S5}$$

$$\frac{1}{G_{12}} = V_f \frac{1}{G_f} + V_m \frac{1}{G_m} \tag{S6}$$

In the above equations, subscripts $\boldsymbol{m}$ and $\boldsymbol{f}$ refer to matrix and fiber (suture), respectively, while V_m and V_f are the associated volume fractions, elaborated upon in the next paragraph. Poisson's ratio of glass and rubber were assumed to be 0.33 and 0.5 according to literature (Cox *et al*, 2019). Shear modulus of the homogeneous glass and rubber are calculated based on experimental Young's moduli:

$$G = \frac{E}{2(1+v)} \tag{S7}$$

In general, fiber laminate theory assumes a uniformly oriented array of fibers (Figure S2a). Since the sine and cosine parameters are squared, however, the orientation of every other fiber is mirrored to form a triangular pattern (Figure S2b) which is used as a simplified analog for the sinusoidal suture (Figure S2c), where the half tooth tip angle of $\boldsymbol{\theta}$ determining the orientation of suture with respect to the load direction is calculated as:

$$\theta = tan^{-1}\left(\frac{\lambda}{2A}\right). \tag{S8}$$

The rectangle bounding the sutures in Figure S2, represents the region where volume fractions are calculated for input into Equation S1. The results are then fed into the spring model where volume fractions are recalculated relating the volume of the homogenized suture region (red rectangle in Figures S2d,e) to that of the entire sample.

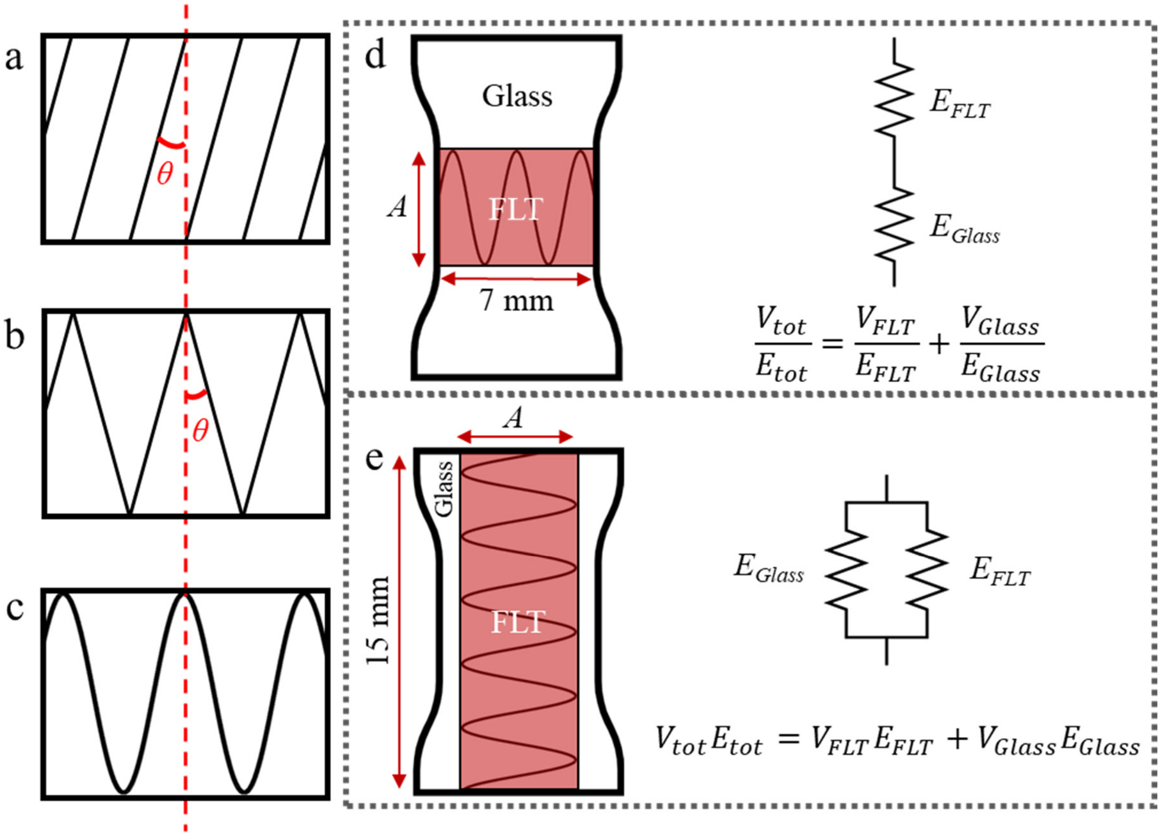

Figure S3. Transforming the a) assumed uniform fiber distribution of fibers in FLT into a b) triangular pattern by mirroring the orientation of every other fiber and assuming the triangular pattern can be equated to c) the sinusoidal suture, so long as the actual interlayer volume used in the FLT equation is still calculated based upon the true sinusoidal suture volume. d) Under perpendicular loading conditions a spring series can be used to predict the bulk sample modulus, E_{tot}, where the stiffness of one spring is determined by FLT (equation S1) and the second spring is represented by the stiffness of the monolithic glassy matrix. e) Under parallel loading conditions the springs are placed in parallel to model bulk response.

Failure of Composite films embedded with a suture joint

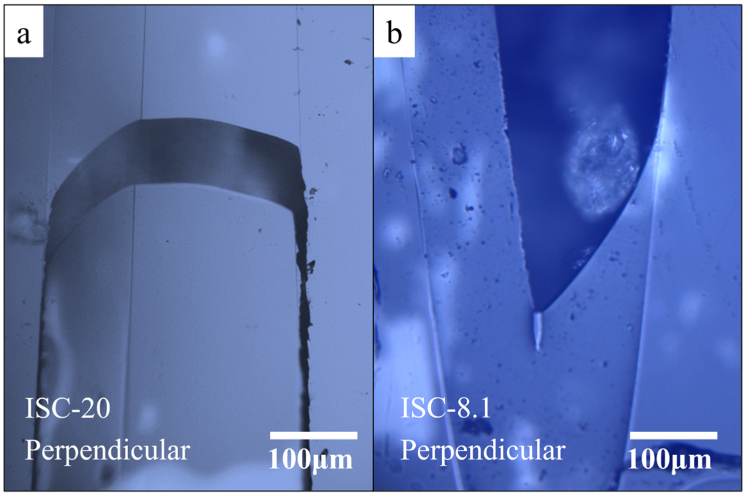

Figure S4. a) Major tooth loss may arise in any suture with an ISC greater than 1, depicted in an ISC-20 suture here. It occurs away from the suture apex and is visible by eye. b) Minor tooth loss was observed in samples with an ISC of 8.1 and larger, depicted in an ISC-8.1 suture here. It occurs within 100 µm of the suture apex and is not visible by eye.

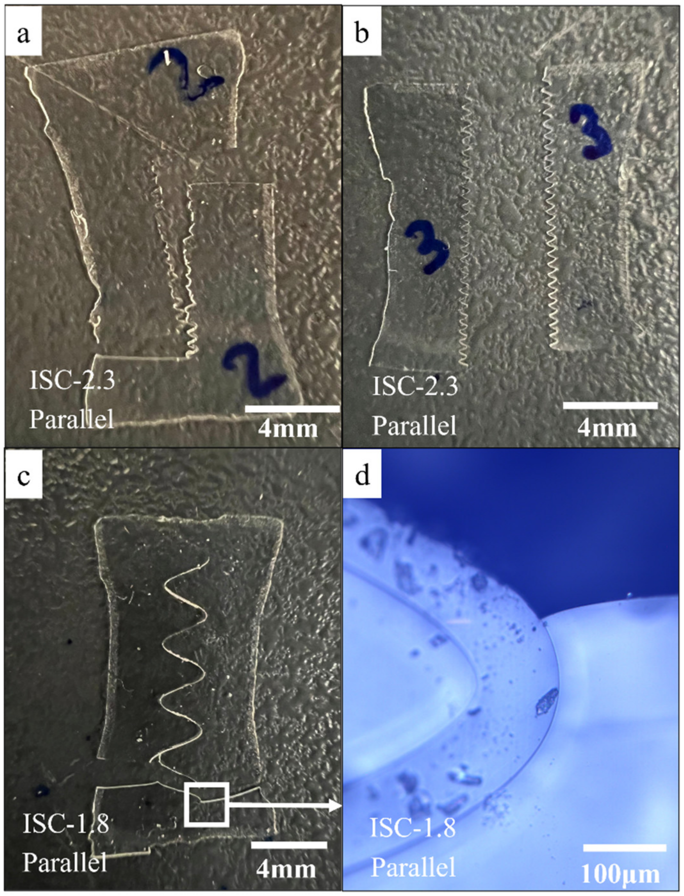

Figure S5. Selected examples of complex crack paths under parallel loading conditions that propagate beyond the neck of the dog bone sample. a) The offset between horizontal crack path segments spans a region slightly larger than the neck of an ISC-2.3 dog bone sample and b) an example of a crack in a different sample with the same geometry that fully interacts with the clamp, the horizontal, bisecting crack paths followed the clamp along the bottom of the sample. c) A crack path in an ISC-1.8 sample appearing just beyond the neck of the dog bone and d) an optical image of the corresponding fracture surface where the crack exits the suture.

Statistical Analysis

The modulus of ISC-3.8 sutured composite showed no statistical difference between the perpendicular and parallel loads (via a two-sample t-test, $t_4 = 1.44$, p-value$= 0.222$).

No difference was observed when comparing the toughness of ISC-20 under perpendicular loads with a pure monolithic glass (via a two-sample t-test, $t_{25} = -0.47$, p-value$= 0.639$).

In addition, no statistical differences observed for strength of ISC-3.8 sutures under the two loading conditions (via a two-sample t-test, $t_4 = -0.04$, p-value$= 0.968$).

For sutures perpendicular to the loading direction, the data suggests a linear relationship between the mechanical properties and ISC, especially for the case of toughness and strength. As a result, single linear regression was used to model the variation of the mechanical properties with ISC as the variable.

$$\frac{E_{ISC}}{E_1} = 0.98 + \ 0.42 \log ISC \tag{S9}$$

$$\log\left(\frac{W_{ISC}}{W_1}\right) = 1.36 \log ISC \tag{S10}$$

$$\frac{\sigma_{ISC}}{\sigma_1} = 0.55 + \ 3.37 \log ISC \tag{S11}$$

Adjusted r-squared values were used to compare the SLR and MLR fitted models obtained for perpendicular suture joints (Table S2). SLR model for modulus had lower accuracy compared to the proposed MLR model, while SLR for both toughness and strength were slightly more accurate than the proposed MLR model for perpendicular conditions. Overall, since two sutures of different amplitudes and wavelengths can have similar ISCs, and for consitensy between the proposed models for parallel and perpendicular loading conditions, we proceeded with MLR models.

Table S2. Adjusted r-squared values of SLR (ISC as the variable) and MLR (amplitude and wavelength as the variables) models for perpendicular loading condition.

Fitting model	Modulus	Toughness	Strength

MLR (A, λ)	Eqn. 2 - 41.18%	Eqn. 4 – 85.74%	Eqn. 6 – 79.85%
SLR (ISC)	Eqn. S9 – 35.70%	Eqn. S10 – 88.90%	Eqn. S11 – 83.46%

Video analysis of failure of sutured composites

ISC-1.0, 1.8, and 20 sutured composites were analyzed through video and synced with the stress-strain curves obtained with DMA, names of the associated MP4 files are indicative of the geometry being tested. All DMA tests were conducted at a strain rate of 2% min^{-1}.